Nanoscale

ROYAL SOCIETY OF CHEMISTRY

PAPER

View Article Online
View Journal | View Issue

Cite this: *Nanoscale*, 2020, **12**, 2752

Nanoparticles decorated with granulocyte-colony stimulating factor for targeting myeloid cells†

Katherine Margulis, ‡[a,b] Alexander Honkala,‡[c] Irina Kalashnikova,[d] Sarah E. Noll,[a] Meghan Hill,[d] Richard N. Zare *[a] and Bryan Ronain Smith *[c,d]

Received 30th July 2019,
Accepted 29th December 2019

DOI: 10.1039/c9nr06494j

rsc.li/nanoscale

Dysregulated myeloid cell activity underlies a variety of pathologies, including immunosuppression in malignant cancers. Current treatments to alter myeloid cell behavior also alter other immune cell subpopulations and nonimmune cell types with deleterious side effects. Therefore, improved selectivity of myeloid treatment is an urgent need. To meet this need, we demonstrate a novel, targeted nanoparticle system that achieves superior myeloid selectivity both *in vitro* and *in vivo*. This system comprises: (1) granulocyte-colony stimulating factor (G-CSF) as a targeting ligand to promote accumulation in myeloid cells, including immunosuppressive myeloid-derived suppressor cells (MDSCs); (2) albumin nanoparticles 100–120 nm in diameter that maintain morphology and drug payload in simulated physiological conditions; and (3) a fluorophore that enables nanoparticle tracking and models a therapeutic molecule. Here, we show that this strategy achieves high myeloid uptake in mixed primary immune cells and that nanoparticles successfully infiltrate the 4T1 triple-negative breast tumor murine microenvironment, where they preferentially accumulate in myeloid cells in a mouse model. Further development will realize diagnostic myeloid cell tracking applications and therapeutic delivery of myeloid-reprogramming drugs.

Introduction

The nature of the myeloid cell response to inflammation, in cancer and other diseases, is a significant determinant of disease outcome and patient health. Myeloid cells are a heterogeneous lineage that include macrophages, dendritic cells, and neutrophils, which mediate inflammatory reactions. Among these are also myeloid-derived suppressor cells (MDSCs),[1–3] a group of immature myeloid cells that strongly suppress the function of CD8+ T-cells and natural killer (NK) T-cells involved in tumor progression and wound healing.[4–6] During an acute inflammatory response, as in the case of pathogen invasion, immature myeloid cells quickly expand and differentiate into monocytes and activated neutrophils, whose activity is determined by the immunological milieu in which they are activated.[7,8] However, during persistent inflammation, as seen in chronic conditions such as many cancers, normal hematopoiesis may be disrupted, resulting in both bone-marrow-based and local myelopoiesis, where accumulated immature myeloid cells are exposed to varied differentiation signals and may instead be converted into MDSCs or other noncanonical myeloid cell sub-types, such as tolerogenic dendritic cells or "M2" macrophages.[5,8–12] These noncanonical myeloid cells exert myriad immunosuppressive functions, which may normally help regulate inflammation at a wound site, but, in the context of cancer, are co-opted to retard the ability of canonical dendritic cells, CD8+ T-cells, and NK T-cells to combat tumor growth and contribute to poor prognosis.[7,12,13] Thus, it is clear that detection of myeloid cell presence, phenotype, and activity at a tumor site is highly important for diagnostic, prognostic, and treatment decision purposes, while inhibition of myeloid-mediated immunosuppressive functions will be a compelling therapeutic strategy with the potential to reduce cancer progression and patient mortality.

In recent years, a number of studies attempting to detect, characterize, modulate, and quantify myeloid cells[5,14–18] have found that the levels and phenotype of myeloid cells in circulation and in the tumor microenvironment at the time of diagnosis are a significant prognostic indicator for disease progression in breast, colorectal, and other cancers.[16,17,19] Presence of MDSCs in the tumor microenvironment also reduces treatment efficacy.[6] Improved detection of myeloid cell levels, phenotype, localization, and activity may have signifi-

[a]*Department of Chemistry, Stanford University, Stanford, CA, 94305, USA. E-mail: zare@stanford.edu*
[b]*The Institute for Drug Research, The School of Pharmacy, Faculty of Medicine, The Hebrew University of Jerusalem, Jerusalem 9112001, Israel*
[c]*Department of Radiology and the Molecular Imaging Program, Stanford University, Stanford, CA, 94305, USA. E-mail: smit2901@msu.edu*
[d]*Department of Biomedical Engineering and the Institute for Quantitative Health Science & Engineering, Michigan State University, East Lansing, MI 48824, USA*
†Electronic supplementary information (ESI) available. See DOI: 10.1039/c9nr06494j
‡These authors contributed equally.

cant impact on treatment design and patient stratification, which demands improved means of measuring, localizing and eventually reprogramming of myeloid cells in patients.

For detection and quantification of myeloid cells, *ex vivo* analysis of blood by flow cytometry has conventionally been used[20] to characterize surface receptors of myeloid cells such as Ly-6C and CD11b in mice. This strategy enables discrimination of certain types of myeloid cells from other, non-immunosuppressive myeloid cell subpopulations, such as mature neutrophils or macrophages.[20,21] However, such detection is limited to peripheral blood or terminal samples and as such is incapable of dynamically tracking myeloid cell migration to tumor loci or modulating their function.

In the present study, we developed targeted fluorescent albumin nanoparticles that label myeloid cells throughout the body to monitor their recruitment into the tumor microenvironment. We employ recombinant granulocyte colony-stimulating factor (G-CSF), a glycoprotein that regulates the migration, proliferation, and functional maintenance of all myeloid cells,[22] as a surface ligand to target these nanoparticles to myeloid cells. This novel and simple approach enables a preferential accumulation of the nanoparticles in myeloid lineage cells and not in other types of cells within the complex tumor microenvironment. Measuring the localization, population size, and/or movement of the myeloid cells in the tumor microenvironment *via* this approach could provide insight into the prognostic outlook of cancer patients while providing a platform to deliver pharmacological agents to these cells for modification of their behavior and to change disease progression.[16,19,23]

Results and discussion

Nanoparticle formation, loading, and characterization

In this study, nanoparticles (NPs) comprising bovine serum albumin were prepared to deliver fluorophores to myeloid cells. The most abundant protein in mammalian blood, albumin, can be used to form NPs with an excellent *in vivo* safety profile.[24] The US Food and Drug Administration (FDA) has recently approved several drug formulations and clinical diagnostic agents based on albumin NPs.[24] This generally facilitates and accelerates the approval and implementation into the clinic of any albumin-based NPs employed for bio-imaging or drug delivery.[24] In this study, NPs were prepared by desolvation of albumin from aqueous solution into an ethanolic phase and subsequent thermal gelation of the NPs followed by the replacement of aqueous medium with phosphate buffered saline (PBS) (1×, pH 7.4). The unloaded NPs had a hydrodynamic diameter of 80 ± 3 nm, determined from the intensity distribution by dynamic light scattering (DLS), and a negative ζ-potential of −15.1 ± 0.6 kV, measured in 0.9% NaCl water solution. Measuring particle size by Scanning Electron Microscopy (SEM) showed that individual dried NP sizes are smaller than those measured by DLS in solution, 40 ± 8 nm in diameter by SEM (Fig. 1A). We first formed albumin NPs by utilizing albumin–fluorescein isothiocyanate conjugates for fluorescence purposes; these NPs were used successfully *in vitro*. However, fluorescein has a strong emission between 500–600 nm, the same wavelength range in which we detected considerable tissue autofluorescence in separate *in vivo* experiments. This hindered our ability to effectively detect myeloid cells with our NPs *in vivo*. To remedy this, we used indocyanine green (ICG), a tricarbocyanine dye that is safe for intravenous administration[25] and approved by the FDA for near-infrared (NIR) optical imaging in humans.[26–30] ICG has an emission maximum at ~800 nm, which allows bio-imaging with minimal autofluorescence interference. ICG exhibits negligible fluorescence in aqueous solution and enhanced fluorescence upon interaction with larger molecules such as proteins, making it an ideal candidate for incorporation into albumin NPs. Furthermore, because of its amphiphilic character, ICG loaded in the NPs can effectively simulate the molecular loading of a variety of myeloid-cell-modulating small molecules, such as celecoxib or sildenafil,[31] many of which present a combination of hydrophilic and lipophilic properties.

As above, ICG was introduced into the aqueous solution of albumin prior to desolvation, and the process resulted in successful incorporation of ICG into the NPs. After thermal dena-

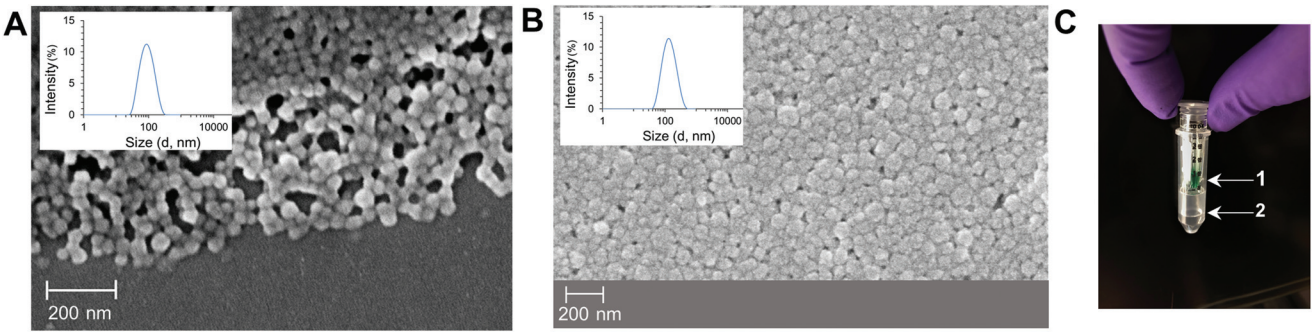

Fig. 1 NP size and loading. (A and B) SEM images of (A) pristine BSA NPs and (B) ICG-loaded NPs (the insets show representative size distribution by DLS); (C) ICG-loaded NPs after multiple washes with PBS by centrifugal filtration using 100 kDa MWCO centrifugal filters: 1. ICG is completely retained in NPs, which are accumulated in the pellet having an intense green color; 2. completely clear filtrate.

turation of NPs and displacement of the medium by PBS, there was no observable leakage of ICG and centrifugal filtration resulted in a completely optically clear supernatant, while the NP-containing pellet had a deep green color (Fig. 1C). The resultant particles had a mean hydrodynamic diameter of 110 ± 4 nm (by intensity distribution, DLS), polydispersity index of 0.24 ± 0.04, ζ-potential of −15.4 ± 0.3 mV (measured in 0.9% NaCl aqueous solution), and they contained 3.3 ± 0.6 wt% ICG. The entrapment efficiency of ICG in the NPs was calculated to be 16.5%. It is important to note that we used an excess of ICG without attempting to maximize its entrapment efficiency. SEM images indicate that dry particles are 67 ± 16 nm in diameter (Fig. 1B).

NP stability and ICG release

NP stability was evaluated at 4 °C for a month. At this temperature, ICG remained tightly bound to albumin NPs dispersed in PBS, as seen in Fig. 2A. The size of these particles was also tracked throughout this period and deviated less than 11% in mean hydrodynamic diameter by intensity as measured by DLS. Strong noncovalent binding stemming from hydrophobic interactions between albumin and ICG[32] likely accounts for this excellent particle stability and negligible fluorophore leakage.

We also measured the release of ICG at 37 °C in 20% fetal bovine serum (FBS) in PBS solution to mimic physiological conditions. The release of ICG is facilitated by elevated temperature and the presence of proteins from FBS in the release medium (Fig. 2B). Nevertheless, the particles retain more than 80% of their ICG load within 5 hours of exposure to biological medium without the significant initial burst release endemic to many other NP formulations.[33] As shown below, this time frame is sufficient for specific accumulation of the NIR dye in the target cells *in vivo* for theranostic purposes.[30]

Ligand conjugation for targeting myeloid cells

Subsequently, G-CSF was covalently linked to the surface of the resultant ICG-loaded NPs using carbodiimide chemistry. G-CSF regulates the activity of myeloid cells and has also been shown to play a crucial role in their generation.[34,35] Recently, depletion of G-CSF by neutralizing or scavenging immunotherapy was proposed as a possible therapeutic route to decrease the MDSC population.[22,34,36] However, the potential side effects of such treatment may include severe neutropenia, vulnerability to infections, and decreased overall anti-cancer immunity.[2] In this study, we used an alternative strategy: we employed G-CSF as a ligand to promote the uptake of ICG-loaded NPs in myeloid cells, exploiting the abundance of G-CSF receptors on the myeloid cell surface and the preservation of ligand–receptor specificity upon N-terminal ligation of G-CSF.[2,37] Such a strategy is compatible with anti-G-CSF treatment or other immunotherapies. Fig. 3A schematically presents the process of G-CSF-conjugated particle formation. Carbodiimide linkage of G-CSF led to a slight increase (22 ± 3%) in the mean hydrodynamic diameter of the resultant NPs, resulting in 141 ± 4 nm diameter with a polydispersity index of 0.17 ± 0.05 (Fig. 3B). The conjugated NPs exhibited excellent storage stability in PBS at 4 °C for 5 weeks with fluctuations in the mean hydrodynamic diameter of less than 9%. They were used for biological experiments within this period of time.

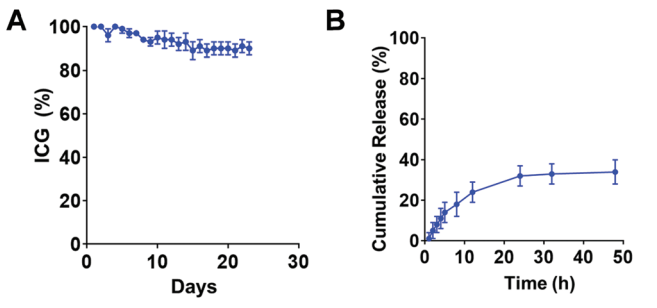

Fig. 2 Stability of NPs. (A) ICG content in NPs in storage at 4 °C in PBS (B) cumulative release from NPs at 37 °C in 20% v/v FBS in PBS solution. NPs do not exhibit an initial "burst release" of payload characteristic of many other nanoparticle formulations.

Cytotoxicity

The cytotoxicity of G-CSF-conjugated as well as unconjugated NPs was tested against the RAW 264.7 macrophage cell line by 3-(4,5-dimethylthiazol-2-yl)-2,5-diphenyltetrazolium bromide (MTT), live/dead cell, and proliferation assays. No statistical difference in cytotoxic effects of conjugated and unconjugated NPs on macrophages were detected within the 0.05–100 ng ml^{-1} concentration range. No change in proliferation capability and rate of macrophages treated with PBS and NPs (conjugated and control) was observed (Fig. S1†).

Myeloid cell uptake

The effect of the G-CSF decoration of NPs was tested in a preliminary experiment conducted in the RAW 264.7 cell line, a macrophage cell line derived from multiple myeloma that consistently expresses the G-CSF receptor (CSF3R).[38] Dispersions of 0.05 ng mL^{-1} or 0.005 ng mL^{-1} decorated or control (undecorated) NPs containing albumin–fluorescein isothiocyanate conjugate were added to the RAW 264.7 cells diluted to 500 000 cells per well. Flow cytometry characterization of cells revealed that G-CSF decoration of the NPs greatly enhanced their uptake into RAW 264.7 cells at each dose tested (Fig. 4A). A micrograph shows RAW 264.7 cell internalization of fluorescein isothiocyanate (FITC)-containing G-CSF decorated NPs (Fig. 4B).

Competitive uptake

A competitive uptake control study demonstrated that G-CSF added to RAW 264.7 cells competed with uptake of ICG-loaded NPs decorated with G-CSF (1.6-fold decrease in NP-G-CSF uptake by RAW 264.7 cells in comparison with control NPs, significance by *T*-test, $P = 0.0014$), suggesting binding is due to the G-CSF conjugated to NPs (Fig. 4C).

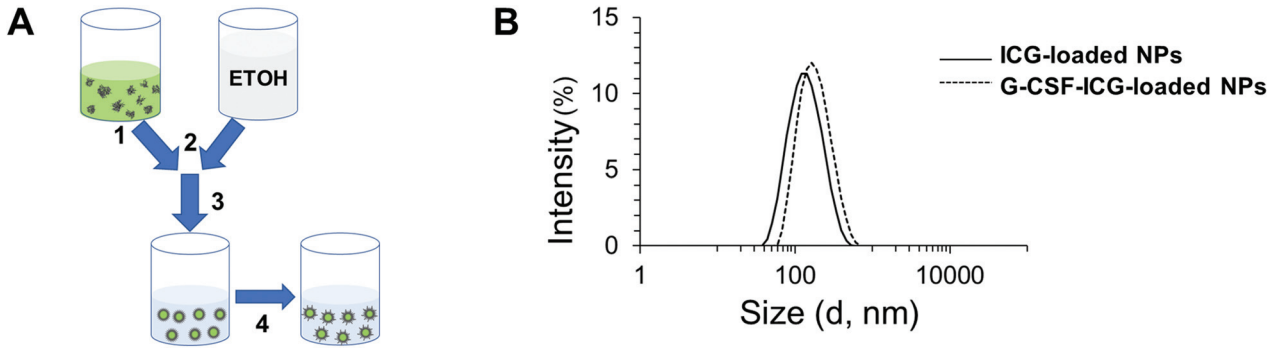

Fig. 3 Ligand conjugation to albumin NPs. (A) Schematic of NP formation process employed in this study: 1. globular protein BSA and water-soluble ICG are dissolved in water; 2. resultant aqueous solution is mixed with an excess of ethanol (EtOH); 3. NPs are formed by albumin desolvation and preserved by thermal denaturation of albumin chains. ICG is incorporated into the particles; 4. G-CSF is attached to the particle surface *via* carbodiimide linkage at pH = 5.5 with subsequent replacement of medium to PBS. Stable NPs are formed. (B) Representative distributions of hydrodynamic diameter of ICG-loaded NPs before (solid line) and after (dotted line) G-CSF linkage.

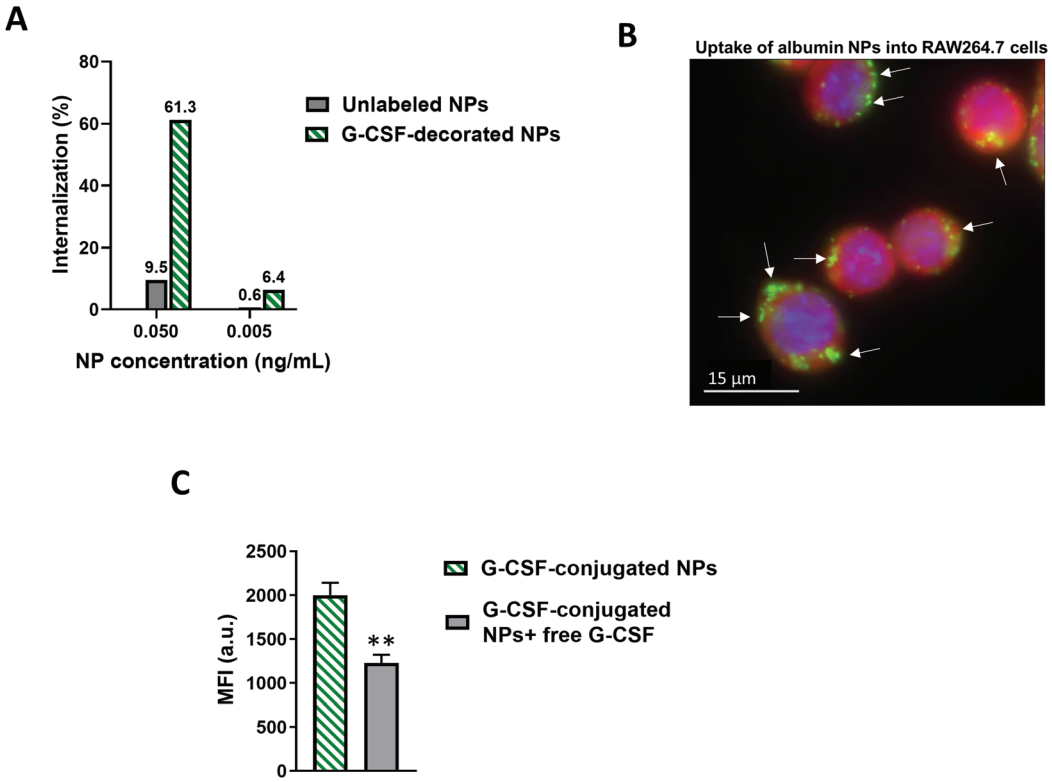

Fig. 4 G-CSF-targeted and undecorated albumin NP uptake by RAW 264.7 cells. A: Inclusion of the G-CSF targeting moiety greatly increased FITC-containing NP uptake by RAW 264.7 multiple myeloma cells, which express the G-CSF receptor. Undecorated control NPs showed limited uptake. Dose amounts are NP mass. B: Internalization of FITC-containing G-CSF decorated NPs into RAW 264.7 cells. Arrows designate NPs. Filters: purple DAPI – nucleus; red TRITC – cell membrane; green FITC – NPs. C: Competitive uptake study shows that G-CSF added to RAW 264.7 cells decreases the uptake of ICG-loaded NPs decorated with G-CSF. MFI – median fluorescence intensity.

Uptake in mixed primary murine splenocytes

We then examined NP uptake specificity *in vitro* in mixed primary murine splenocytes containing T-cells, B-cells, NK cells, macrophages, neutrophils, dendritic cells, and MDSCs isolated from both tumor-free and 4T1 triple negative breast cancer-bearing mice. MDSCs are normally a rare cell population at <5% of circulating peripheral blood mononuclear cells (PBMCs). The 4T1 murine breast cancer model reliably increases MDSC populations in the blood, spleen, and tumor microenvironment within 10 days of implantation. Thus, 4T1 tumor-bearing mouse splenocytes contain many more MDSCs

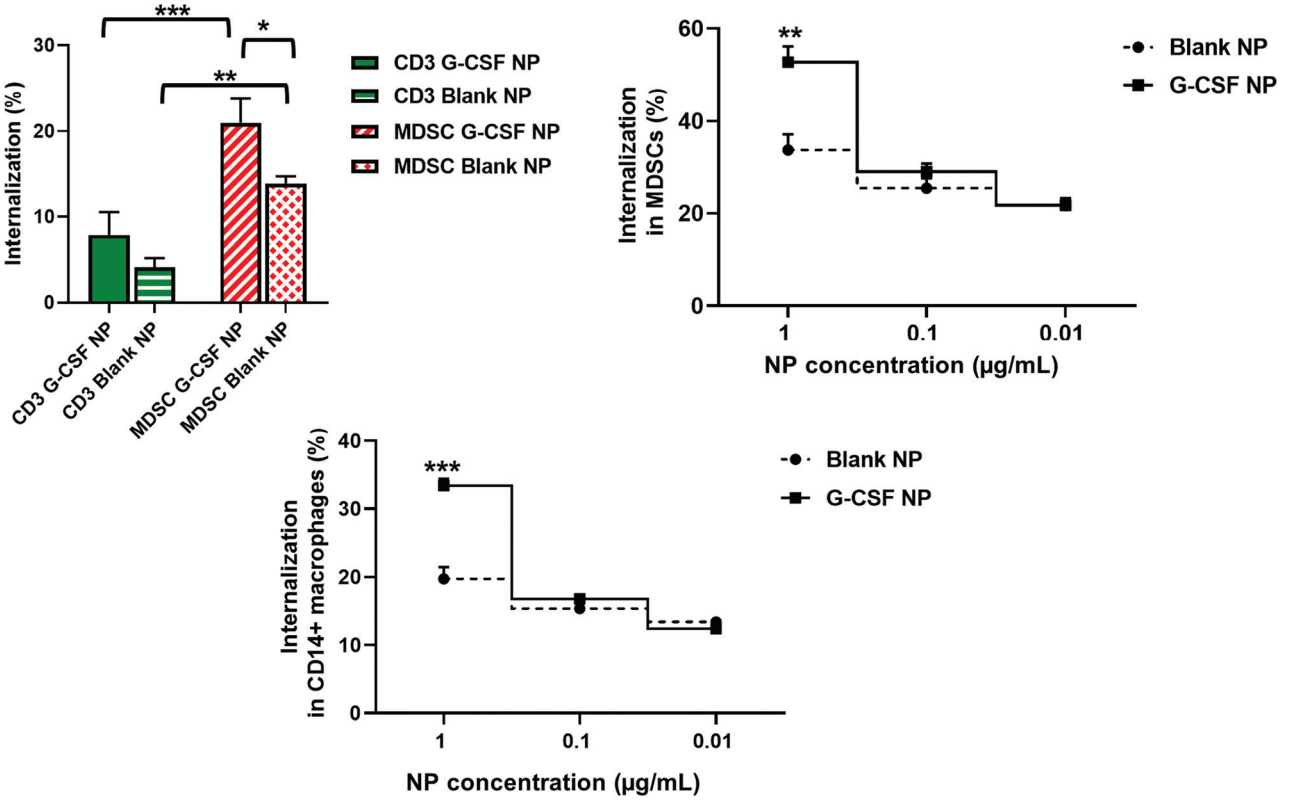

Fig. 5 NP selectivity in mixed splenocytes. Primary immune cells were isolated from the spleens of 4T1 breast cancer-bearing immunocompetent Balb/c mice. 4T1 was implanted in the mammary fat pad *via* subcutaneous injection and allowed to grow for 10 days before primary cell isolation. In each study, splenocytes were plated at 100 000–250 000 cells per well and treated with varying doses of G-CSF-decorated and undecorated albumin NPs bearing ICG to track internalization. After 30 minutes of incubation, cells were washed and prepared for flow cytometry, which measured NP internalization *via* emission >800 nm as well as several cell surface markers indicative of immune cell subpopulations. A: Incubation of 1 μg FITC-labeled NPs showed that G-CSF decorated and undecorated NP controls both accumulate in MDSCs at much higher levels than in CD3+ T-cells, in which limited nonspecific uptake is seen. Inclusion of the G-CSF targeting moiety significantly increased MDSC uptake. MDSCs were defined as CD11b+/Ly6C+ or CD11b+/Ly6G+ and macrophages were defined as CD14+. Statistical significance by one-way ANOVA with the Bonferroni *post-hoc* analysis, $*P \leq 0.033$, $**P \leq 0.002$, $***P < 0.001$. B and C: G-CSF decoration again increased NP uptake in MDSCs in a significant and dose-dependent manner, also demonstrating some uptake in CD14+ macrophages. NPs used here were labeled with indocyanine green (ICG), which improved uptake detection. Statistical significance by *t*-test, $*P < 0.05$, $**P < 0.01$, $***P < 0.001$.

than tumor-free mice.[39] Mixed splenocytes were exposed for 30 minutes to various concentrations of NPs in media. Across all experiments and conditions, G-CSF decoration of the NPs greatly increased myeloid cell uptake, including uptake into MDSCs (Fig. 5). Limited nonspecific uptake into less than 10% of total CD3+ T-cells was also observed, although G-CSF decoration did not significantly increase NP uptake into CD3+ cells, suggesting that nonspecific uptake of albumin NPs occurs in a limited proportion of cells. Uptake of these NPs into MDSCs was significantly higher ($P = 0.0044$), and G-CSF decoration increased the uptake (Fig. 5A). It can be seen in Fig. 5B that decorated NPs achieved above 50% accumulation in MDSCs and above 30% accumulation in CD14+ non-MDSC macrophages (Fig. 5C), showing differential accumulation and the potential to preferentially label or alter myeloid cells. NP uptake was defined as cells emitting fluorescence at >800 nm as a result of ICG internalization after removal of NP-containing medium and 3× washes in PBS.

NP uptake *in vivo*

Finally, we tested the effect of G-CSF decoration of NPs on cell specificity *in vivo* in 4T1 tumor-bearing mice. A 10 μg bolus dose of ICG-loaded NPs suspended in 100 μL sterile PBS was injected *via* tail vein in anesthetized mice and the NP distribution was then imaged using the Lago X (Spectral Instruments Imaging) *in vivo* imaging system. Images were taken at 0, 30, and 180 minutes after NP administration. At 180 minutes, mice were sacrificed to harvest spleen, liver, and tumor. Harvested tissues were processed into single-cell suspensions, which were then fixed and prepared for flow cytometry in triplicate. Results showed that G-CSF-decorated NPs accumulated in MDSCs at significantly higher rates compared to undecorated (blank) NPs in the spleen and tumor microenvironment (TME) ($P < 0.001$ Fig. 6A and B). On the other hand, 4T1 tumor-bearing mouse livers took up all NPs at significantly lower rates than did tumor-free mouse livers, which displayed increased uptake of nanoparticles regardless of

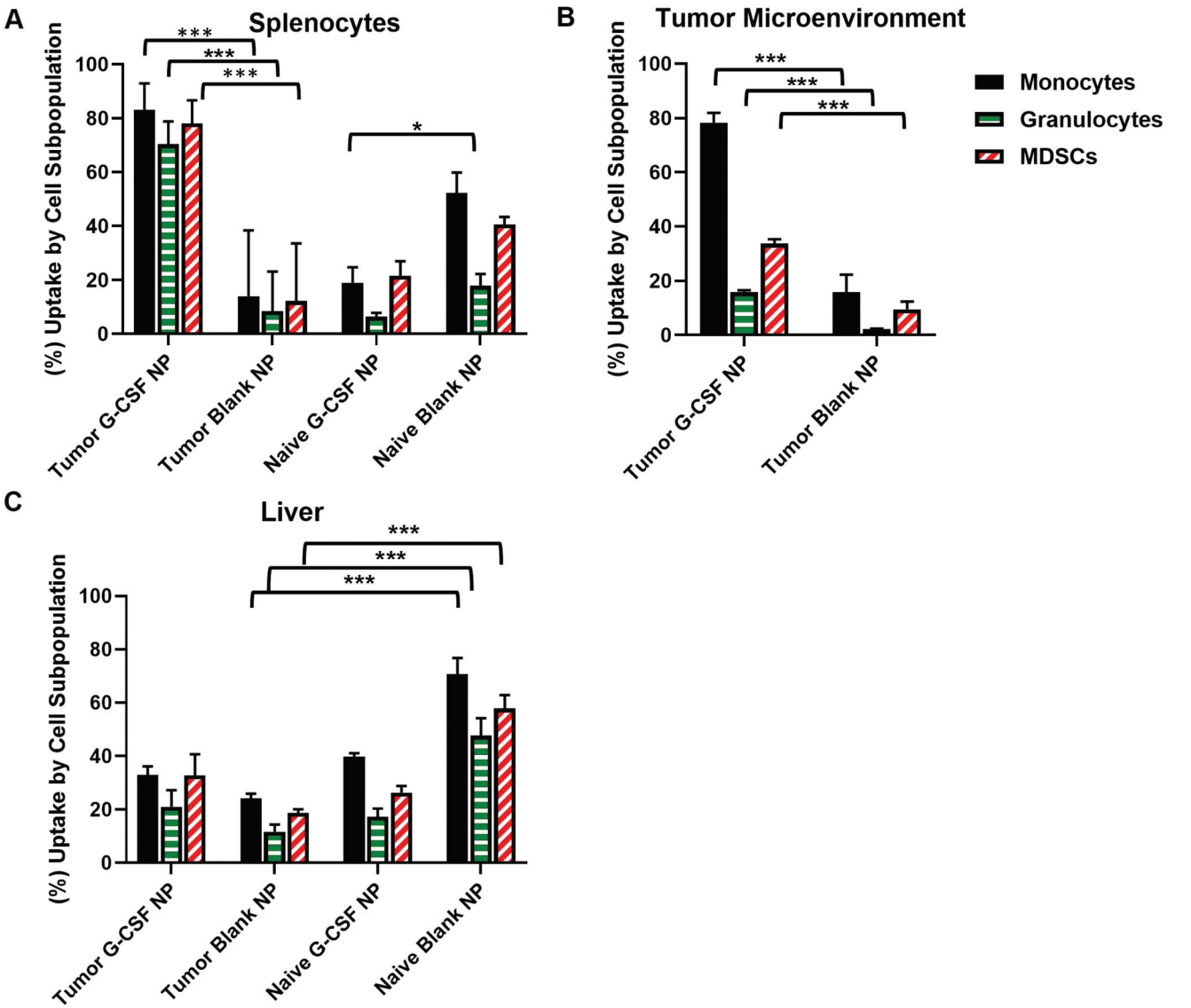

Fig. 6 NP uptake *in vivo*. 10 μg of G-CSF-decorated and undecorated albumin NPs were each injected into separate groups of mice. One group of mice was tumor-naïve and the other group had been inoculated with 4T1 cells in the mammary glands 10 days before the experiment, during which they grew to ~500 mm^3. All NPs were labeled with indocyanine-green (ICG), which permitted visualization of NP distribution *via in vivo* fluorescence imaging and measurement of NP uptake by cell type *via* flow cytometery post-sacrifice. All samples were taken 3 hours after NP injection. A: Characterization of the spleen showed that NPs were taken up by Ly6C+ monocytes, Ly6G+ granulocytes, and dual-positive Ly6C+/Ly6G+ immature MDSCs, wherein G-CSF decoration significantly enhanced NP uptake. These trends were not observed for undecorated control NPs in tumor-bearing mice or for either undecorated or G-CSF-decorated NPs in tumor-free mice. B: The same trend was seen in the 4T1 tumor microenvironment, where G-CSF decoration significantly enhanced uptake into each myeloid cell subpopulation. C: In the liver, G-CSF decoration did little to increase NP uptake when compared with undecorated controls. Interestingly, more NPs were taken up by cells in the liver in tumor-free mice than in 4T1-tumor-bearing mice, suggesting that either fewer NPs were available for internalization or tumor growth alters the composition or activation states of myeloid cells within the liver in a manner that alters their propensity to internalize NPs, decorated or not. Statistical significance by two-way ANOVA with the Bonferroni *post-hoc* analysis, $*P \leq 0.033$, $**P \leq 0.002$, $***P < 0.001$.

surface decoration; this finding is likely indicative of homeostatic mononuclear phagocyte system activity that is altered in tumor-bearing hosts[40] (Fig. 6C). These data demonstrate that G-CSF decoration of albumin NPs is an effective strategy to achieve preferential myeloid and MDSC accumulation *in vivo* where specificity effects are enhanced in the tumor-bearing mice *vs*. tumor-free mice. Furthermore, these data also indicate that albumin NPs can effectively circulate through the bloodstream into myeloid cells within the tumor microenvironment, as shown by NP accumulation in ~70% of monocytes and ~35% of MDSCs isolated from the 4T1 tumor microenvironment, so that effective delivery is achieved even if some portion of NPs is taken up by the mononuclear phagocyte system.

Discussion

Improving the selectivity of myeloid tracking and reprogramming is a key to effective treatment of immunologically active cancers and other conditions. In this study, we show that decoration of small molecule-bearing albumin NPs with recombinant G-CSF is not only reproducibly formulable and stable in a variety of conditions, but also increases preferential uptake into myeloid cells both *in vitro* in a cell line and in mixed immune cells from tumor-naïve as well as 4T1 metastatic triple-negative breast cancer-bearing mice (in which MDSCs and other immunosuppressive myeloid cells play a deleterious role by promoting disease progression and treatment resistance).[41] This trend was also observed *in vivo*, where G-CSF-decorated NPs effectively accumulated in myeloid cells in the liver, spleen, and tumor microenvironment within just 3 hours at much greater rates than control undecorated NPs, which displayed nonspecific uptake regardless of tumor condition. This study was performed as a proof-of-concept in one mouse per condition: 4T1-tumor bearing and non-tumor bearing mice to test vehicle control of ICG in PBS, unlabeled NP, and G-CSF-conjugated NP. By achieving accumulation in more than 50% of all monocytes and more than 20% of MDSCs in the 4T1 tumor microenvironment, G-CSF-decorated NPs provide substantial insight into the levels of local myeloid cell presence *via* accumulation in a significant proportion thereof in a single dose. All NPs tested *in vivo* were labeled with ICG, providing an optimized strategy to assess cell subpopulation uptake and overall distribution throughout the body *via* the Lago X imaging system (Fig. 7). While ICG alone (vehicle control) disseminated widely throughout the body, NPs loaded with ICG localized more to spleen, liver, and peri-tumoral regions. Intriguingly, at 180 minutes post-injection, NPs displayed a more concentrated anatomical profile in 4T1-bearing mice, indicative of localization in the tumor or liver, whereas non-tumor-bearing mice showed greater disseminated spread of NPs, regardless of surface decoration. These results may be indicative of altered mononuclear phagocyte system clearance in tumor-bearing hosts, and these issues invite close observation and assessment in future studies investigating quantitative NP biodistribution and pharmacokinetics.

These data provide proof-of-concept for a new nanoparticle-based diagnostic imaging method, in which the ICG-labeled, G-CSF-targeted albumin NPs could be used to approximate myeloid cell infiltration into the tumor microenvironment as a marker of diagnosis, prognosis, or treatment response.[16,19,42,43,44–49] Furthermore, by showing effective complexation of indocyanine green, an amphiphilic dye, with the albumin nanoparticle, we paved the way to test loading of drug molecules with the potential to alter myeloid cell behavior as part of a novel therapeutic strategy with the potential to overcome limitations inherent to previous systemic approaches.[50–52]

Future perspectives

Key limitations of this study include: (a) the limited characteristics of the immune cells and cancer types profiled, where deeper flow cytometry characterization or other tumor models may provide greater insight into the potential of these NPs for diseases other than breast cancer; (b) testing only ICG complexation to NPs, the protocols for which may require alteration to load other small molecules; and (c) the potential for G-CSF receptor binding to drive undesired myeloid cell biology. Future studies will explore each of these aspects and determine the effective dose–exposure relationship between injected NPs and NPs accumulating in myeloid cells in the TME.

Further development of the system reported here may enable cell lineage-specific delivery of ICG as an effective photothermal and photosensitizing agent for combined photothermal/photodynamic therapy of cancer; ICG is known as a robust photothermal and photoacoustic imaging agent.[29,30,53–59] When ICG is delivered to a certain population of cells and concentrated within them, it is capable of converting NIR light into localized heat and toxic chemical species (such as reactive oxygen species and singlet oxygen) resulting in cell destruction.[26,53–55] This approach could be adopted to reduce or reprogram the population of myeloid cells in the tumor microenvironment for highly immunosuppressed patients. This NP system could also be used for photoacoustic imaging of immune cell distributions in patients, for the delivery of immune-modulatory small molecules and subsequent alteration of the innate immune system, or even as a potent

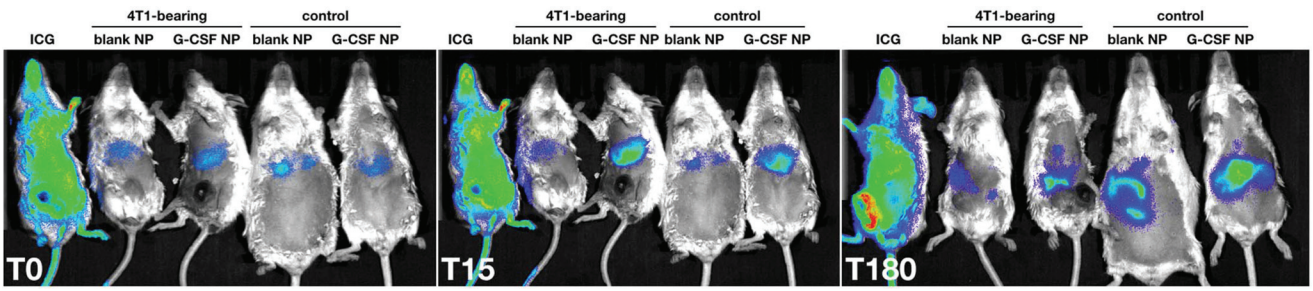

Fig. 7 Tumor microenvironment study. To test the effect of G-CSF decoration of NPs on biodistribution and tumor MDSC accumulation, we injected 10 μg each of ICG alone, blank NP, and G-CSF-NPs in 100 μL PBS into either 4T1 breast carcinoma-bearing or tumor-free mice and imaged the shaved mice using a >800 nm filter using the Lago X fluorescent imaging system at 0 (T0, left), 15 (T15, center), and 180 (T180, right) minutes after administration. Tumor, spleen, and liver NP accumulation by cell type were assayed by flow cytometry (Fig. 6).

theranostic agent to measure and reprogram myeloid cells. Eventual application of this system to the clinic, which may be accelerated given that all NP components have been FDA-approved, could yield vital treatment monitoring information for immuno-oncological applications and, with small molecule drug payloads, could provide an immunomodulatory platform for myeloid cell reprogramming in a variety of pathologies.

Experimental

Materials

BSA (average M_w 66.0 kDa, ≥96%) was purchased from Sigma-Aldrich, BSA–fluorescein isothiocyanate (FITC) conjugate with molar ratio of FITC/BSA ≥ 7 and BSA average M_w 66.0 kDa was obtained from Sigma-Aldrich, ICG was from Sigma, recombinant murine G-CSF (19.0 kDa) was obtained from PeproTech, PBS (1×, pH 7.4), sodium hydroxide 1 N, ethanol, and biological grade water were purchased from Fisher Scientific.

BSA nanoparticle formation and ICG loading

NPs were formed by dissolving BSA 5 wt% in water adjusted to pH = 9 by NaOH, with subsequent desolvation of albumin by gradual addition of ethanol 1 : 4 v/v. To stabilize the NPs and prevent albumin dissociation, the resultant mixture was subjected to 3 rounds of mild heating (70 °C for 10 minutes) to denature free albumin chains within the NPs. To load the NPs with ICG, an excess of ICG (1 wt%) was dissolved in water at pH = 9 with 4 wt% BSA as above. The desolvation and particle denaturation steps above were unchanged. The NPs with incorporated ICG were then washed with an excess of PBS to remove unincorporated dye and to displace the medium with a biologically compatible one. Washing was performed by centrifugal filtration at 10 000 rpm for 5 min in an Eppendorf 5415 C Centrifuge using a 100 kDa MWCO EMD Millipore Amicon™ Ultra-0.5 centrifugal filter units. Washing was repeated thrice, resulting in a completely clear filtrate, and the nanoparticle-containing pellet was deep green. NPs were stored at 4 °C, protected from light.

For the formation of BSA–FITC NPs in our preliminary experiments (Fig. 4A and B), BSA–FITC conjugate was dissolved at 5 wt% in PBS. This was followed by a gradual desolvation/heat denaturation process when overall 170 wt% of anhydrous ethanol was added to the solution followed by several short (overall 15 min) NP denaturation cycles at 70° C. NPs were then washed with excess PBS by centrifugal filtration as described above, stored at 4 °C, and protected from light.

Nanoparticle characterization

NP size was assessed in PBS dispersion by dynamic light scattering (DLS). The size distribution was measured at room temperature using a Nano-ZS90 Zetasizer (Malvern, UK) equipped with a 632.8 nm laser source. The same instrument was used to evaluate NP ζ-potential, however for these measurements the media was replaced with 0.9% water solution of NaCl to avoid affecting electrophoretic mobility by the high concentration of electrolytes in the media. Each measurement was performed in triplicate in three independent samples.

The size and morphology of the resultant dry NPs was corroborated by high-resolution SEM. For these measurements, the PBS in the medium was replaced with deionized water by three washes using centrifugal filtration as above, and the resultant dispersion was diluted 1 : 50 with deionized water. It was then deposited onto 15 mm aluminum SEM stubs and allowed to air-dry overnight. All samples were gold–palladium sputter-coated with a Denton Desk II sputter-coater (Denton Vacuum, Moorestown, NJ). SEM imaging was carried out by a high-resolution Zeiss Sigma field emission scanning electron microscope (FESEM) (Zeiss Microscopy, Thornwood, NY) operated at an accelerating voltage of 2–3 kV using InLens Secondary Electron (SE) detection, and 5–7 kV using Backscattered Electron Detection (BSD). Images were captured in TIFF using storage resolution 2048 × 1536 pixels and a line averaging noise reduction algorithm. To determine NP size from SEM images, we processed three SEM images using ImageJ software by selecting areas with even illumination.[60] N = 153 optimally illuminated unloaded and N = 198 ICG-loaded NPs were measured for size estimation.

ICG concentration was determined by UV-vis spectroscopy using an absorbance microplate reader (Azure Biosystems, Dublin, USA) with a 750 nm filter. Specifically, the ICG-loaded NP dispersion after washing, or the filtrate collected from centrifugal filtration, was diluted with known excess volumes of 50% v/v aqueous dimethyl sulfoxide (DMSO) solution and sonicated for 15 min to extract the ICG from denatured albumin. Absorbance was then measured, and the concentration was calculated using a standard calibration curve for ICG. To assess particle stability, the concentration of ICG was monitored by aliquoting the dispersion, performing centrifugal filtration as above, and measuring the ICG concentration in the pellet. Similarly, for release experiments, the ICG content inside the dialysis tubes was determined from independent samples exposed to release for different time intervals. This minimized the potential error of free ICG degradation in aqueous solution over time. NP fluorescence was monitored using a TECAN infinite M1000 plate reader (Männedorf, Switzerland) and fluorescence microscope (DMRXE, Leica, Germany). NP concentration was calculated in weight of particles per volume. These numbers were based on the albumin weight and estimation of albumin molecule number in each particle calculated by the particle size.

G-CSF conjugation

The NPs were covalently linked to G-CSF using carbodiimide chemistry based on amide bond formation between BSA chains and G-CSF protein under mild aqueous conditions with a zero-length crosslinker that leaves no residues in the resultant protein.[61] Briefly, a 20 μg per 100 μL solution of G-CSF was activated with 5 mM of EDC (1-ethyl-3-(3-dimethylaminopropyl)carbodiimide hydrochloride)/sulfo-NHS (sulfo-*N*-hydroxysuccinimide) at pH = 5.5 and the NP dispersion medium was adjusted to pH 5.5 by NaOH addition. Both solu-

tions were then united and kept at 4 °C for 4 hours protected from light. The approximate molar mixed ratio between G-CSF and NPs was 10 : 1. NPs were then dialyzed against PBS for 18 h at 4 °C using Pur-A-Lyzer™ dialysis tubes (MWCO 6–8 kDa, Sigma-Aldrich) protected from light.

Cytotoxicity tests

MTT assay. RAW 264.7 cells (3000 cells per well) were seeded in 96-well plates for 24 h. The cells were then incubated with 100 μl of G-CSF-conjugated and unconjugated NPs at a concentration range of 0.05–100 ng ml^{-1} in cell culture medium without phenol red for 24 h at 37 °C. Appropriate controls (cell culture medium and 0.1%Triton X-100 (v/v)) were also used. Cells were then rinsed twice with PBS, and incubated with 100 μl of 0.5 mg ml^{-1} of MTT reagent dispersed in cell culture medium without phenol red for 3.5 h at 37 °C. The assay was completed by aspirating the MTT reagent and adding 100 μl of DMSO. Shaking the plate for 15 min at room temperature on the orbital shaker helped dissolve formazan crystals. The optical density in each well was determined at 550 nm (MTT assay).

Live/dead cell analysis by flow cytometry. RAW 264.7 cells were seeded (300 000 cells per ml) in 6-well plates overnight and then treated with different concentrations of G-CSF conjugated and unconjugated NPs in cell culture medium for 24 h. Afterward, culture medium was aspirated, and cells were rinsed twice with PBS, and detached with trypsin/EDTA solution. The cell pellet was resuspended in PBS and stained on ice with Zombie yellow dye at 1 : 500 dilution for 20 minutes. After staining, cells were washed twice with 1 mL of flow wash buffer (1% BSA + PBS + 0.1% sodium azide), and fixed with 500 μL of 1% paraformaldehyde in PBS for 30 minutes on ice. After that, 1 ml of flow wash buffer was added to each tube and cells were centrifuged at 1000 rpm using a Sorvall ST 8R centrifuge with TX-150 rotor (Thermo Fisher Scientific) for 5 minutes at 4 °C. Before analysis, cell pellets were resuspended in 300 μL of flow wash buffer and filtrated using Flowmi tip strainers (70 μm). The samples were analyzed with a Cytek Aurora™ (Cytek Biosciences) cytometer.

Proliferation assay. RAW 264.7 cells at 80% confluency were detached by trypsin/EDTA solution, rinsed twice with PBS, and stained with CellTrace violet (Thermo Fisher) at 1 : 500 dilution per 1×10^6 cells for 30 min at room temperature. After that, cells were washed twice with cell culture medium without phenol red and seeded in 6-well plates. Stained cells were treated with G-CSF conjugated and unconjugated NPs in cell culture medium for 48 h, with 10 μg ml^{-1} cycloheximide for 4 h, and with PBS. Cells proliferated for 72 h in total and then were detached, rinsed with PBS and stained with Zombie NIR (1 : 500 dilution) for 30 min on ice. After staining, cells were washed twice with 1 ml of flow wash buffer, and fixed with 500 μl of 1% paraformaldehyde in PBS for 30 minutes on ice. Afterward, 1 ml of flow wash buffer was added to each tube and cells were centrifuged at 1000 rpm using Sorvall ST 8R centrifuge with TX-150 rotor (Thermo Fisher Scientific) for 5 minutes at 4 °C. Before analysis, cell pellets were resuspended in 300 μl of flow wash buffer and filtrated using a Flowmi tip strainer (70 μm). The samples were analyzed with the Cytek Aurora™.

Competitive uptake control study

RAW 264.7 cells at 80% confluency were spun down, seeded at 500 000 cells per well to a round-bottom 96-well plate, and then treated with 0.05 ng mL^{-1} G-CSF conjugated and unconjugated NPs in presence or absence of G-CSF (0.5 ng ml^{-1}). Cells were pre-incubated with G-CSF for 30 min at 37 °C and then incubated with NPs for 90 minutes, spun down at 1000 rpm using a Sorvall ST 8R centrifuge with TX-150 rotor (Thermo Fisher Scientific) for 5 minutes to aspirate supernatant containing non-internalized NPs, washed once in PBS to remove remaining non-internalized NPs, placed on ice, and stained with propidium iodide. Samples were filtrated using Flowmi tip strainer (70 μm) and analyzed with a BD FACS ARIA IIu™ (BD Biosciences).

RAW 264.7 internalization

The RAW 264.7 myeloid cell line (a gracious gift from the Leeper laboratory at Stanford University, Department of Cardiovascular Medicine) was cultured in standard Dulbecco's Modified Eagle Medium (DMEM) with 10% fetal bovine serum. RAW 264.7 cells at 70% confluency were spun down, washed in PBS, diluted to 500 000 cells per well in a round-bottom 96-well plate, and then were added to standard DMEM containing 0.05 ng mL^{-1} or 0.005 ng mL^{-1} decorated or control (undecorated) NPs containing albumin–fluorescein isothiocyanate conjugate. Cells with NPs were incubated at 37 °C for 90 minutes then spun down at 1100 rpm for 3 minutes to aspirate supernatant containing noninternalized NPs, washed once in PBS to remove remaining noninternalized NPs, and then fixed in 5% formalin, and stained with propidium iodide. NP uptake was then quantified *via* flow cytometry as described below.

Imaging of BSA–FITC G-CSF decorated NPs uptake within RAW 264.7 cells

RAW 264.7 cells were plated at 50 000 cells per well in an 8-well slide (Ibidi) and left overnight at 37 °C under a humidified atmosphere containing 5% CO_2. Cells were then stained using 0.4 μg mL^{-1} Hoechst 33342 trihydrochloride, trihydrate (Thermo Fisher Scientific) and 0.5 μM CellTracker Orange CMRA (Thermo Fisher Scientific) suspended in PBS. After staining, 5 μg mL^{-1} of FITC-containing G-CSF decorated NPs suspended in cell culture medium without phenol red were added to each well and incubated at 37 °C for 90 minutes. Following incubation, cells were washed with PBS, and, after washing, the PBS was aspirated and replaced with cell culture medium without phenol red. Finally, cells were imaged using a DeltaVision by Applied Precision Inc. microscope (GE Healthcare Life Sciences) with DAPI, TRITC, and FITC filters and an Olympus 60×/1.42, Plan Apo N, UIS2, 1-U2B933 objective. Images were obtained with an EDGE/sCMOS_5.5 camera and Resolve 3D softWoRX-Acquire Version 7.0.0 software. Pixel size is 0.1077 μm.

Bulk splenocyte uptake

Bulk splenocytes containing mixed T-cells, B-cells, and myeloid cells were isolated from wild-type Balb/c mice *via* surgical harvest of the spleen in both 4T1 triple negative breast cancer-bearing mice—which is known to induce more MDSCs—and tumor-free mice. Splenocytes were extracted *via* maceration of the spleen in PBS followed by filtration through a 70 μm nylon cell filter, washing the well in which the spleen was macerated with PBS through the cell filter up to 20 mL to increase yield. Cells were then spun down at 1100 rpm for 3 minutes, followed by removal of the supernatant and incubation in 5 mL of ACK Lysis Buffer at room temperature for 5 minutes. Subsequently, the cells were spun down again and resuspended in PBS for quantification of cell yield *via* hemocytometer. Bulk splenocytes were then plated into 96-well round-bottom plates in standard Roswell Park Memorial Institute (RMPI) culture medium at 250 000–500 000 cells per well. Aliquots containing ICG-labeled NPs were prepared at 2× their final concentration (1 μg, 100 ng, 10 ng) in RPMI and then diluted 2-fold in each well of a 96 well plate. NPs tested included non-G-CSF-decorated NPs as well as G-CSF-decorated NPs. Splenocytes were incubated at 37 °C in RPMI containing NPs for 30 minutes, after which they were spun down, washed once in PBS, and resuspended in 10% formalin for fixation and flow cytometric characterization.

Tumor microenvironment study

4T1 tumor-bearing mice were prepared *via* subcutaneous implantation of 10^5 4T1 cells in the right mammary flank of female Balb/c mice and allowed to grow for 10 days, by which point tumors were palpable and ~0.5–1 cm in diameter. Mice were then anesthetized *via* isofluorane inhalation and placed in the imaging chamber of a Lago X, (Spectral Instruments Imaging) and administered 10 μg of ICG-labeled NPs suspended in 100 μL of sterile PBS *via* tail vein. Both G-CSF-decorated NPs and undecorated NPs were tested. Lago X images were taken at the time of administration and again at 3.5 hours post-injection, at which point mice were sacrificed. Then tumor, liver, and spleen were harvested. Each tissue was macerated, with tumor enzymatically digested in collagenase IV solution, to prepare single-cell suspensions that were then fixed in 10% formalin prior to flow cytometric analysis.

Live subject statement

All animal procedures were approved by the Stanford University Institutional Animal Care and Use Committee and conformed to the NIH guidelines for the use of laboratory animals.

Flow cytometry

Fixed cells suspended in PBS were spun down at 1100 rpm for 3 minutes and resuspended in blocking buffer (3% bovine serum albumin, 10% fetal bovine serum in PBS) and incubated on ice for 30 minutes. Dilutions of fluorophore-conjugated commercially-available antibodies (Bio-Rad, Lonza, Thermo Fisher) were prepared in the same buffer. Fixed cells were spun down, supernatant removed, and antibodies were then incubated on ice for another 30 minutes. Cells were then spun down and washed in PBS three times prior to flow cytometric analysis on a Luminex Guava easyCyte cytometer. Flow cytometry was performed within 4 days of fixing cells. All analysis was done with FlowJo, where NP-positive cells were counted as those emitting NIR fluorescence from ICG-NPs as a percentage of all counted cells, not as an absolute quantification of NPs per cell.

Conflicts of interest

There are no conflicts to declare.

Acknowledgements

The authors are grateful to the AACR (American Association for Cancer Research) and BCRF (Breast Cancer Research Foundation) for the Translational Breast Cancer Award (17-20-26-SMIT) funding to support this work (BRS and RZ). We thank Niloufar Hosseini-Nassab and Xingjun Zhu for their help and discussions with this study.

References

1 D. I. Gabrilovich, V. Bronte, S.-H. Chen, M. P. Colombo, A. Ochoa, S. Ostrand-Rosenberg and H. Schreiber, *Cancer Res.*, 2007, **67**, 425–425.
2 P. Trikha and W. E. Carson 3rd, *Biochim. Biophys. Acta*, 2014, **1846**, 55–65.
3 C. Travelli, F. M. Consonni, S. Sangaletti, M. Storto, S. Morlacchi, A. A. Grolla, U. Galli, G. C. Tron, P. Portararo, L. Rimassa, T. Pressiani, M. Mazzone, R. Trovato, S. Ugel, V. Bronte, C. Tripodo, M. P. Colombo, A. A. Genazzani and A. Sica, *Cancer Res.*, 2019, **79**, 1938–1951.
4 T. Condamine and D. I. Gabrilovich, *Trends Immunol.*, 2011, **32**, 19–25.
5 V. Fleming, X. Hu, R. Weber, V. Nagibin, C. Groth, P. Altevogt, J. Utikal and V. Umansky, *Front. Immunol.*, 2018, **9**, 398.
6 A. Stiff, P. Trikha, B. Mundy-Bosse, E. McMichael, T. A. Mace, B. Benner, K. Kendra, A. Campbell, S. Gautam, D. Abood, I. Landi, V. Hsu, M. Duggan, R. Wesolowski, M. Old, J. H. Howard, L. Yu, N. Stasik, T. Olencki, N. Muthusamy, S. Tridandapani, J. C. Byrd, M. Caligiuri and W. E. Carson, *Clin. Cancer Res*, 2018, **24**, 1891–1904.
7 C. Murdoch, M. Muthana, S. B. Coffelt and C. E. Lewis, *Nat. Rev. Cancer*, 2008, **8**, 618–631.
8 D. I. Gabrilovich, *Cancer Immunol. Res.*, 2017, **5**, 3–8.
9 M. Nahrendorf and F. K. Swirski, *Circ. Res.*, 2016, **119**, 414–417.
10 F. O. Martinez and S. Gordon, *F1000Prime Rep.*, 2014, **6**, 13.

11 A. Sica and L. Strauss, *J. Leukocyte Biol.*, 2017, **102**, 325–334.
12 F. Leonard, L. Curtis, M. Ware, T. Nosrat, X. Liu, K. Yokoi, H. B. Frieboes and B. Godin, *Front. Immunol.*, 2017, **8**, 693.
13 X. Z. Ye, S. C. Yu and X. W. Bian, *J. Genet. Genomics*, 2010, **37**, 423–430.
14 O. De Henau, M. Rausch, D. Winkler, L. F. Campesato, C. Liu, D. H. Cymerman, S. Budhu, A. Ghosh, M. Pink, J. Tchaicha, M. Douglas, T. Tibbitts, S. Sharma, J. Proctor, N. Kosmider, K. White, H. Stern, J. Soglia, J. Adams, V. J. Palombella, K. McGovern, J. L. Kutok, J. D. Wolchok and T. Merghoub, *Nature*, 2016, **539**, 443–447.
15 A. Florcken, A. Takvorian, A. Singh, A. Gerhardt, B. N. Ostendorf, B. Dorken, A. Pezzutto and J. Westermann, *Immunol. Lett.*, 2015, **168**, 260–267.
16 J. Galon, A. Costes, F. Sanchez-Cabo, A. Kirilovsky, B. Mlecnik, C. Lagorce-Pages, M. Tosolini, M. Camus, A. Berger, P. Wind, F. Zinzindohoue, P. Bruneval, P. H. Cugnenc, Z. Trajanoski, W. H. Fridman and F. Pages, *Science*, 2006, **313**, 1960–1964.
17 A. J. Gentles, A. M. Newman, C. L. Liu, S. V. Bratman, W. Feng, D. Kim, V. S. Nair, Y. Xu, A. Khuong, C. D. Hoang, M. Diehn, R. B. West, S. K. Plevritis and A. A. Alizadeh, *Nat. Med.*, 2015, **21**, 938.
18 B. R. Smith, E. E. B. Ghosn, H. Rallapalli, J. A. Prescher, T. Larson, L. A. Herzenberg and S. S. Gambhir, *Nat. Nanotechnol.*, 2014, **9**, 481.
19 R. F. Gabitass, N. E. Annels, D. D. Stocken, H. A. Pandha and G. W. Middleton, *Cancer Immunol. Immunother.*, 2011, **60**, 1419–1430.
20 S. Kitano, M. A. Postow, C. G. Ziegler, D. Kuk, K. S. Panageas, C. Cortez, T. Rasalan, M. Adamow, J. Yuan, P. Wong, G. Altan-Bonnet, J. D. Wolchok and A. M. Lesokhin, *Cancer Immunol. Res.*, 2014, **2**, 812–821.
21 M. Sade-Feldman, J. Kanterman, Y. Klieger, E. Ish-Shalom, M. Olga, A. Saragovi, H. Shtainberg, M. Lotem and M. Baniyash, *Clin. Cancer Res*, 2016, **22**, 5661–5672.
22 W. Li, X. Zhang, Y. Chen, Y. Xie, J. Liu, Q. Feng, Y. Wang, W. Yuan and J. Ma, *Protein Cell*, 2016, **7**, 130–140.
23 P. Chhour, P. C. Naha, S. M. O'Neill, H. I. Litt, M. P. Reilly, V. A. Ferrari and D. P. Cormode, *Biomaterials*, 2016, **87**, 93–103.
24 F.-F. An and X.-H. Zhang, *Theranostics*, 2017, **7**, 3667–3689.
25 J. T. Alander, I. Kaartinen, A. Laakso, T. Patila, T. Spillmann, V. V. Tuchin, M. Venermo and P. Valisuo, *Int. J. Biomed. Imaging*, 2012, **2012**, 940585.
26 Z. Sheng, D. Hu, M. Xue, M. He, P. Gong and L. Cai, *Nano-Micro Lett.*, 2013, **5**, 145–150.
27 S. L. Gibbs, *Quant. Imaging Med. Surg.*, 2012, **2**, 177–187.
28 R. Tivony, L. Larush, O. Sela-Tavor and S. Magdassi, *J. Biomed. Nanotechnol.*, 2014, **10**, 1041–1048.
29 Y.-G. Wang, H. Kim, S. Mun, D. Kim and Y. Choi, *Quant. Imaging Med. Surg.*, 2013, **3**, 132–140.
30 S. H. Hong, H. Kim and Y. Choi, *Nanotechnology*, 2017, **28**, 185102.
31 M. G. Lechner and A. L. Epstein, *Clin. Cancer Res*, 2011, **17**, 1645–1648.
32 M. Nairat, A. Konar, M. Kaniecki, V. V. Lozovoy and M. Dantus, *Phys. Chem. Chem. Phys.*, 2015, **17**, 5872–5877.
33 X. Huang and C. S. Brazel, *J. Controlled Release*, 2001, **73**, 121–136.
34 S. I. Abrams and J. D. Waight, *OncoImmunology*, 2012, **1**, 550–551.
35 M. Kawano, S. Mabuchi, Y. Matsumoto, T. Sasano, R. Takahashi, H. Kuroda, K. Kozasa, K. Hashimoto, A. Isobe, K. Sawada, T. Hamasaki, E. Morii and T. Kimura, *Sci. Rep.*, 2015, **5**, 18217.
36 F. Shojaei, X. Wu, X. Qu, M. Kowanetz, L. Yu, M. Tan, Y. G. Meng and N. Ferrara, *Proc. Natl. Acad. Sci. U. S. A.*, 2009, **106**, 6742–6747.
37 B. B. Yang and A. Kido, *Clin. Pharmacokinet.*, 2011, **50**, 295–306.
38 Q. Zhang, C. C. Fong, Y. Zhang, C. H. Tzang, W. F. Fong and M. Yang, *Life Sci.*, 2008, **82**, 135–148.
39 B. A. Pulaski and S. Ostrand-Rosenberg, *Current protocols in immunology*, 2001, ch. 20, Unit 20.22.
40 T. M. Saba, *Arch. Intern. Med.*, 1970, **126**, 1031–1052.
41 J. E. Talmadge and D. I. Gabrilovich, *Nat. Rev. Cancer*, 2013, **13**, 739–752.
42 B. R. Smith and S. S. Gambhir, *Chem. Rev.*, 2017, **117**, 901–986.
43 S. Cole, A. Montero, E. Garret-Mayer, G. Onicescu, T. Vandenberg, S. Hutchens and C. Diaz-Montero, *Cancer Res.*, 2009, **69**, 4135.
44 A. J. Montero, C. M. Diaz-Montero, C. E. Kyriakopoulos, V. Bronte and S. Mandruzzato, *J. Immunother.*, 2012, **35**, 107–115.
45 R. Wesolowski, J. Markowitz and W. E. Carson 3rd, *J. Immunother. Cancer*, 2013, **1**, 10.
46 S. Solito, I. Marigo, L. Pinton, V. Damuzzo, S. Mandruzzato and V. Bronte, *Ann. N. Y. Acad. Sci.*, 2014, **1319**, 47–65.
47 L. Bracci, G. Schiavoni, A. Sistigu and F. Belardelli, *Cell Death Differ.*, 2014, **21**, 15–25.
48 F. De Sanctis, S. Solito, S. Ugel, B. Molon, V. Bronte and I. Marigo, *Biochim. Biophys. Acta*, 2016, **1865**, 35–48.
49 S. Ostrand-Rosenberg and C. Fenselau, *J. Immunol.*, 2018, **200**, 422–431.
50 X. Ni, G. Hu and X. Cai, *Crit. Rev. Food Sci. Nutr.*, 2018, 1–10, DOI: 10.1080/10408398.2018.1509201.
51 G. S. Karagiannis, J. M. Pastoriza, Y. Wang, A. S. Harney, D. Entenberg, J. Pignatelli, V. P. Sharma, E. A. Xue, E. Cheng, T. M. D'Alfonso, J. G. Jones, J. Anampa, T. E. Rohan, J. A. Sparano, J. S. Condeelis and M. H. Oktay, *Sci. Transl. Med.*, 2017, **9**, eaan0026.
52 R. M. Connolly, M. A. Rudek and R. Piekarz, *Future Oncol.*, 2017, **13**, 1137–1148.
53 B. M. Barth, E. I. Altinoglu, S. S. Shanmugavelandy, J. M. Kaiser, D. Crespo-Gonzalez, N. A. DiVittore, C. McGovern, T. M. Goff, N. R. Keasey, J. H. Adair, T. P. Loughran Jr., D. F. Claxton and M. Kester, *ACS Nano*, 2011, **5**, 5325–5337.

54 C. Shirata, J. Kaneko, Y. Inagaki, T. Kokudo, M. Sato, S. Kiritani, N. Akamatsu, J. Arita, Y. Sakamoto, K. Hasegawa and N. Kokudo, *Sci. Rep.*, 2017, **7**, 13958.
55 K. Tamai, T. Mizushima, X. Wu, A. Inoue, M. Ota, Y. Yokoyama, N. Miyoshi, N. Haraguchi, H. Takahashi, J. Nishimura, T. Hata, C. Matsuda, Y. Doki, M. Mori and H. Yamamoto, *Mol. Cancer Ther.*, 2018, **17**, 1613–1622.
56 M. Fadel, N. Samy, M. Nasr and A. A. Alyoussef, *Pharm. Dev. Technol.*, 2017, **22**, 545–550.
57 W. Li, X. Guo, F. Kong, H. Zhang, L. Luo, Q. Li, C. Zhu, J. Yang, Y. Du and J. You, *J. Controlled Release*, 2017, **258**, 171–181.
58 T. Luo, Q. Zhang and Q. B. Lu, *Cancers*, 2017, **9**, 63.
59 Y. Wang, C. Wang, Y. Ding, J. Li, M. Li, X. Liang, J. Zhou and W. Wang, *Colloids Surf., B*, 2016, **148**, 533–540.
60 C. A. Schneider, W. S. Rasband and K. W. Eliceiri, *Nat. Methods*, 2012, **9**, 671–675.
61 N. Nakajima and Y. Ikada, *Bioconjugate Chem.*, 1995, **6**, 123–130.